PHOTONICS Research

Widely tunable ultra-narrow-linewidth dissipative soliton generation at the telecom band

Chang Kyun Ha,[1] Ki Sang Lee,[1] Dohyeon Kwon,[2] and Myeong Soo Kang[1,*]

[1]Department of Physics, Korea Advanced Institute of Science and Technology (KAIST), Daejeon 34141, South Korea
[2]School of Mechanical and Aerospace Engineering, Korea Advanced Institute of Science and Technology (KAIST), Daejeon 34141, South Korea
*Corresponding author: mskang@kaist.ac.kr

Received 24 January 2020; revised 23 March 2020; accepted 30 March 2020; posted 1 May 2020 (Doc. ID 389080); published 4 June 2020

Ultra-narrow-linewidth mode-locked lasers with wide wavelength tunability can be versatile light sources for a variety of newly emergent applications. However, it is very challenging to achieve the stable mode locking of substantially long, anomalously dispersive fiber laser cavities employing a narrowband spectral filter at the telecom band. Here, we show that a nearly dispersion-insensitive dissipative mode-locking regime can be accessed through a subtle counterbalance among significantly narrowband spectral filtering, sufficiently deep saturable absorption, and moderately strong in-fiber Kerr nonlinearity. This achieves ultra-narrow-linewidth (a few gigahertz) nearly transform-limited self-starting stable dissipative soliton generation at low repetition rates (a few megahertz) without cavity dispersion management over a broad tuning range of wavelengths covering the entire telecom C-band. This unique laser may have immediate application as an idealized pump source for high-efficiency nonlinear frequency conversion and nonclassical light generation in dispersion-engineered tightly light-confining microphotonic/nanophotonic systems.

https://doi.org/10.1364/PRJ.389080

1. INTRODUCTION

Mode-locked lasers emitting a stable optical pulse train are essential as versatile light sources in diverse fields ranging from fundamental sciences to industrial applications. There is an ongoing trend for mode-locked fiber lasers (MLFLs) to be substituted for the existing solid-state counterparts, as the former have several advantages such as freedom from careful alignment and maintenance, excellent environmental stability and reliability, and compactness, which permit robust and cost-effective laser operations [1]. It is accordingly crucial to suitably design the fiber laser cavity to make it ideal for each specific application. A rarely studied but potentially important class of fiber lasers is ultra-narrow-linewidth MLFLs, which are highly attractive for a variety of newly emerging applications, e.g., nonlinear-Fourier-spectrum-based optical communications [2], spectrally encoded photonic quantum information processing [3], generation and control of multiphoton-entangled optical frequency combs [4], high-resolution nonlinear microscopy and spectroscopy [5], reconfigurable nonlinear optical poling of photonic waveguides [6], and efficient coupling of photons to single molecules [7]. In particular, there has been rapidly growing interest in pulsed lasers that can be exploited as pump sources for high-efficiency nonlinear frequency conversion [8–13] and nonclassical light generation [4,14–17] in microscaled/nanoscaled dispersion-engineered long-length photonic waveguide systems, such as microstructured optical fibers [8], optical micro/nano-fibers [9,10,14–16], and nano-scaled on-chip waveguides [11–13,17]. While these systems can provide compact platforms for high-quality nonlinear optical imaging and novel types of photonic quantum information processing, they require more sophisticated characteristics of pump pulses, in addition to the ultra-narrow spectral widths (a few gigahertz or below). The laser wavelength should be tunable over a broad spectral range for precise control of the pump wavelength within the phase-matching bandwidth. Moreover, the pump pulse widths need to be moderately long (a few tens to a few hundred picoseconds) to mitigate the dispersion-induced temporal walk-off effect in the long waveguides, and at the same time have the low repetition rates (a few megahertz or below) favorable for high pulse energy generation. However, while such widely tunable ultra-narrow-linewidth MLFLs are seemingly simple to implement by constructing a long fiber laser cavity that incorporates an intracavity tunable narrowband spectral filter, it has long been regarded as very challenging to achieve self-starting stable mode locking of such fiber laser cavities, particularly at the telecom band (~1550 nm) in the anomalous dispersion regime. Narrow-linewidth MLFLs employing a narrowband fiber Bragg grating have been demonstrated almost exclusively in the all-normal-dispersion regime [18–26]. Furthermore, they have not fulfilled all the desired pulse properties, suffering from severely limited wavelength tunability [18–20,22–26], relatively broad pulse spectra [21–26] and large frequency chirps [26], and

undesirably high repetition rates (tens or hundreds of megahertz) [21–23]. While some experiments on narrow-linewidth mode locking at the telecom band have been recently reported, they still exhibit relatively high repetition rates (~10 MHz) and insufficient wavelength tuning ranges [27–29], and their underlying mode-locking mechanism has not been adequately clarified yet.

In this paper, we report the first (to our knowledge) experimental demonstration of a widely tunable ultra-narrow-linewidth MLFL that generates a nearly transform-limited stable soliton train at the telecom band, which satisfies all the requirements mentioned earlier. While a substantially long telecom single-mode fiber (SMF) delay line (>100 m) is incorporated to lower the pulse repetition rate down to a few megahertz, the self-starting stable single-pulse state can be accessed even with the resultant considerably anomalous cavity dispersion. Compared to all the relevant previous works [27–29], pulse-breakup-free continuous wavelength tuning is achieved over a markedly broad range of 34.3 nm (1529.3–1563.6 nm). This tuning range not only covers almost the entire telecom C-band but is also finally sufficient, particularly for nonlinear frequency conversion and nonclassical light generation in micro-scaled/nanoscaled photonic waveguide systems. Furthermore, the critical pulse parameters such as the pulse width and linewidth can be controlled within the range of 100–150 ps and 2–8 GHz, respectively, by simply changing the pump power. It is revealed from our rigorous numerical modeling, together with experimental investigations, that the remarkable feature of ultra-narrow-linewidth soliton generation with a capability of wide and simple tuning of all pulse parameters, even from a considerably long fiber cavity, is nearly insensitive to the cavity dispersion. This enables our demonstration at the telecom band, where the laser cavity is highly anomalously dispersive, and any kind of cavity dispersion management is unnecessary for stable mode locking, while the cavity dispersion has long been considered an essential physical parameter that governs the soliton formation [30]. Instead, it turns out that the self-starting soliton generation relies critically on the subtle counterbalance among three intracavity actions in both the temporal and spectral domains: significantly narrowband filtering and associated local pulse stretching [31], sufficiently deep saturable absorption and associated spectral broadening, and appropriately adjusted Kerr-nonlinearity-induced spectral broadening in the long fiber cavity. This is in sharp contrast to the case of conventional soliton mode locking, where dispersion-induced pulse broadening plays a crucial role and provides balance against the in-fiber Kerr nonlinearity [30].

2. RESULTS AND DISCUSSION

An MLFL is constructed in a unidirectional ring cavity configuration, as illustrated schematically in Fig. 1. A 0.7-m-long section of erbium-doped fiber (EDF; LIEKKI Er110-4/125) is used as a gain medium, which is pumped by a 976 nm cw laser diode through a wavelength-division multiplexer. The passive mode locking is achieved by incorporating a semiconductor saturable absorber mirror (SESAM) as a saturable absorber. A fiber polarization controller is placed in front of the SESAM to adjust the intracavity polarization state. We employ

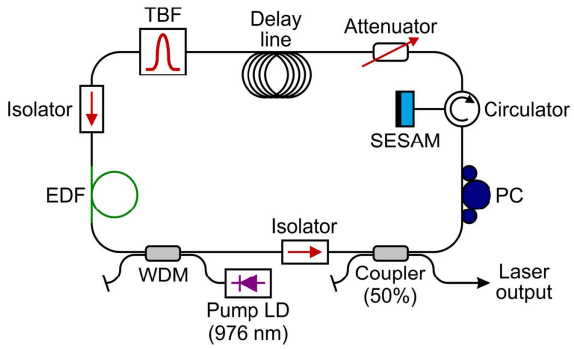

Fig. 1. Schematic diagram of the widely tunable ultra-narrow-linewidth passively mode-locked erbium fiber laser. LD, laser diode; WDM, wavelength division multiplexer; EDF, erbium-doped fiber; TBF, tunable bandpass filter; SESAM, semiconductor saturable absorber mirror; PC, polarization controller.

an ultra-narrowband tunable bandpass filter (TBF; WL Photonics) with a fixed bandwidth of 0.11 nm (14 GHz) and a center wavelength that is continuously variable over the range of 1500–1600 nm. A strand of telecom SMF [$\beta_2 = +17$ ps/(km · nm) at 1550 nm wavelength] is inserted as a delay line to reduce the pulse repetition rate to a few megahertz. An attenuator is placed right before the fiber delay line to properly adjust the optical Kerr effect in the fiber to suppress Kerr-induced pulse breakup [32,33]. The laser output is obtained via a 50/50 tapping coupler, which is located right after the EDF, where the pulse energy is maximized, and the laser linewidth is close to its minimum, as we will discuss later.

We first select an SMF delay line length of 80 m, a SESAM modulation depth of 25%, and an attenuator loss of –4 dB (60%). When the pump power exceeds the laser mode-locking threshold of 265 mW, self-starting stable mode locking is successfully achieved at a fundamental repetition rate of 2.02 MHz (corresponding to the total cavity length of ~100 m), as shown in Figs. 2(a)–2(d). We measure the pulse width to be around 100 ps by using a conventional second-harmonic-generation-based intensity autocorrelator (Femtochrome Research, FR-103WS) with a 400 ps scan range, assuming a sech^2 pulse shape [Fig. 2(b)]. As the autocorrelator scan range is not sufficient to verify the single-pulse laser operation, we monitor the laser output with a 23-GHz-bandwidth high-speed photodetector (ALPHALAS UPD-15-IR2-FC) and a 20-GHz-bandwidth sampling oscilloscope (Agilent 86100A) to check the single-pulse operation by confirming that there is no parasitic pulse in the vicinity of the main pulse. At the same time, since the spectral measurement of ultra-narrow-linewidth optical pulses with a conventional grating-based optical spectrum analyzer is limited by its resolution bandwidth (0.05 nm in our case) [Fig. 2(e)], we observe the optical pulse spectrum by employing the high-resolution heterodyne technique [29]. Here we use a frequency-tunable single-mode cw laser light as a local oscillator (LO) and form a beat note between the laser pulses and the LO, which is detected with the high-speed photodetector and then observed with an electrical spectrum analyzer. Figure 2(f) displays a typical heterodyne electrical spectrum, which can be obtained by carefully adjusting the LO frequency

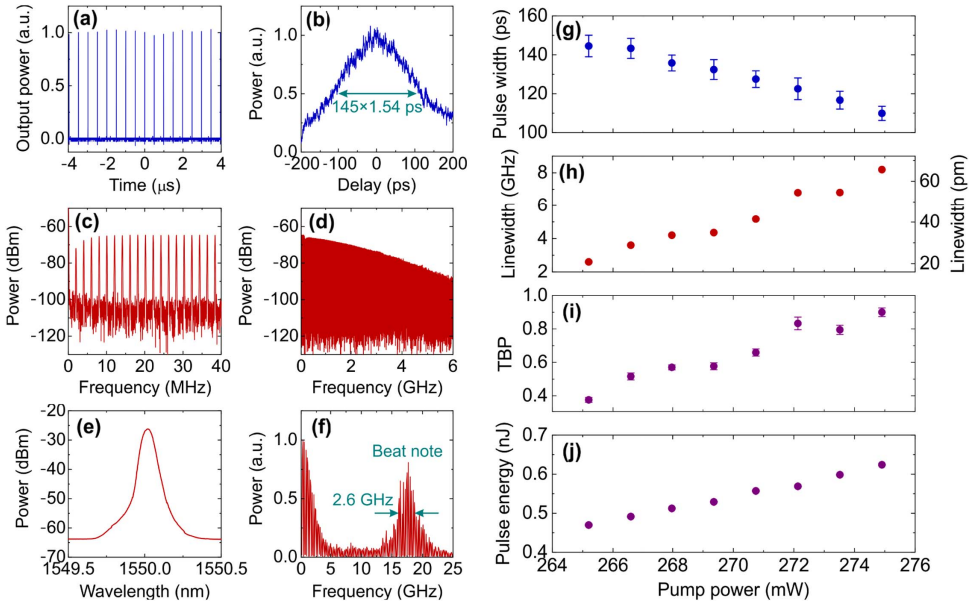

Fig. 2. Characterization of the laser output. (a) Oscilloscope trace, (b) intensity autocorrelation. Note that the width of the autocorrelation trace is larger than the actual pulse width by a factor of 1.54 for sech^2-shaped pulses. Although the autocorrelation trace is slightly asymmetric due to a minor imperfection in our intensity autocorrelator that appears around the +200 ps bound of the scan range, such asymmetry does not hinder the reliable determination of the pulse width. (c) Electrical spectrum over a narrower frequency span (40 MHz), (d) electrical spectrum over a wider frequency span (6 GHz), (e) optical spectrum measured with a grating-based optical spectrum analyzer with a resolution bandwidth of 0.05 nm, (f) high-resolution optical spectrum obtained from the electrical spectrum of the beat note (peaking at 17.5 GHz in this case) that is formed by a continuous-wave local oscillator and the laser output. In (a)–(f), the pump power is fixed at 265.2 mW. (g)–(j) Pump power dependence of the laser output parameters: (g) pulse width, (h) linewidth, (i) time–bandwidth product (TBP), (j) pulse energy. The pulse width is determined from the intensity autocorrelation signal in (b), assuming a sech^2 pulse shape. The linewidth is determined from the electrical spectrum of the beat note in (f). Each error bar represents the standard deviation of 20 repeated measurements. The laser center wavelength is fixed at 1550 nm for all measurements.

at 15–20 GHz away from the center frequency of the laser pulses. Since the LO linewidth (200 kHz) is much smaller than that of the laser pulses, the electrical spectrum of the beat note represents the optical spectrum of the laser pulses. The measured laser linewidth is typically on the order of several gigahertz and can be reduced to 2.6 GHz, which is smaller than previously reported values for all-fiber MLFLs operating in the telecom band [27,28,34]. The resulting time–bandwidth product (TBP) is as low as 0.37, which is very close to the transform-limited value of 0.315 for sech^2 pulses. Although we do not actively stabilize the relative frequency of the LO to the center frequency of laser pulses, the beat note electrical spectrum is sufficiently stable to precisely determine the laser linewidth. We note that the linewidth of the laser pulses is too narrow and their repetition rate is too low to accurately measure the optical pulse spectrum with a scanning Fabry–Perot interferometer [34].

We can access this highly stable self-starting ultra-narrow-linewidth single-pulse state over a range of pump powers. Furthermore, the pulse parameters can be widely tuned by adjusting the pump power, as summarized in Figs. 2(g)–2(j). As the pump power rises, the pulse width is shortened, while the laser linewidth is broadened. The resulting TBP decreases as the pump power falls, while the output pulse energy typically lies at the sub-nanojoule level. These pump power dependences can be understood from the self-phase-modulation (SPM)-induced frequency chirp at the fiber delay line and the spectral filtering at the TBF. Beyond the pump power range for the single-pulse state, a multi-pulse state emerges due to the multi-pulsing instability. In this regime, a single high-energy pulse becomes unstable, as the SPM is too highly accumulated in the fiber delay line, which gives rise to the pulse breakup at the TBF [32,33]. While the operating pump power range of ~10 mW (265–275 mW) that we achieve may be insufficient for some applications, we anticipate that the use of a low-nonlinearity fiber delay line [25] could broaden the operating range of pump power.

We theoretically analyze and design the laser system to optimize the laser performance and explore the mechanism underlying soliton formation in the cavity in detail. We employ the lumped cavity model that treats each element in the laser cavity separately, rather than the distributed model based on the Haus master equation [35], for more rigorous study of the action of individual intracavity components on the propagating optical pulse. For each fiber segment, we solve the nonlinear Schrödinger equation,

$$\frac{\partial A(z,t)}{\partial z} = -\frac{\alpha}{2}A - i\frac{\beta_2}{2}\frac{\partial^2 A}{\partial t^2} + i\gamma|A|^2 A, \tag{1}$$

using the conventional split-step Fourier method [36]. Here, $A(z,t)$ is the slowly varying complex field amplitude, α is the attenuation coefficient, β_2 is the second-order dispersion, and γ is the effective nonlinear coefficient. Most of the

cavity is anomalously dispersive ($\beta_2 = -21.7$ ps^2/km, $\gamma = 1.3$ km/W, and $\alpha = 0.2$ dB/km), except for the EDF ($\beta_2 = +2.85$ ps^2/km and $\gamma = 2.9$ km/W). The EDF gain is expressed as the following saturated gain model [32]:

$$g(\Omega) = \frac{g_0}{1 + \frac{P}{P_S} + \frac{\Omega^2}{\Delta_g^2}}, \tag{2}$$

where g_0, P_S, and Δ_g are the small-signal gain coefficient, saturation power, and gain bandwidth, respectively, of the EDF. Ω is the optical frequency, and the average input power (P) is given as the product of the input pulse energy and the pulse repetition rate. The transmission spectrum of the intracavity bandpass filter is set as a Gaussian function with 1.3 dB insertion loss. The SESAM is modeled by the following rate equation for the power-dependent loss (q) [33]:

$$\frac{\partial q(t)}{\partial t} = -\frac{q - q_0}{\tau} - \frac{|A(t)|^2}{E_S} q. \tag{3}$$

The parameters of SESAM can be experimentally quantified regardless of cavity birefringence, in contrast to the nonlinear polarization rotation. Here, we use the experimentally determined values for the modulation depth, relaxation time, and saturation energy as $q_0 = 0.25$, $\tau = 12$ ps, and $E_S = 30$ μJ/cm^2, respectively, together with a non-saturable loss of 0.17. We calculate the instantaneous power-dependent loss (q) at every temporal position on the pulse.

We numerically obtain the steady-state single-pulse solution at properly adjusted cavity parameters by iteratively applying Eqs. (1)–(3) with the use of a very weak pulse having 1 fW peak power as an initial seed. Figures 3(a) and 3(b) display typical profiles of the output laser pulse solutions in the temporal and the spectral domain, respectively, from which we determine four fundamental pulse parameters—the pulse width, linewidth, TBP, and pulse energy. We then examine the gain dependence of each pulse parameter over a range of small-signal gain coefficient (g_0) values, as shown in Figs. 3(c)–3(f). It is revealed that these pulse parameters are widely tunable without pulse breakup. We obtain a stable single-pulse state above a certain gain threshold ($g_0 = 11.7$ dB in this case). As the gain coefficient rises, the pulse width decreases and the linewidth increases monotonically. In addition, the pulse gets more chirped at higher gain coefficients due to the SPM, yielding larger values of TBP. When the small-signal gain coefficient increases beyond a certain upper limit ($g_0 = 13.2$ dB in this case), multi-pulsing instability hinders the laser from oscillating in the stable single-pulse state, and the laser enters the multi-pulse regime. In this case, a single high-energy pulse becomes unstable as the nonlinear phase modulation is too highly accumulated in the delay line, which gives rise to the pulse breakup at the bandpass filter [32,33]. All these numerical results agree well with our experimental observation in Figs. 2(g)–2(j) and show a similar tendency to the previously reported cases in the all-normal dispersion regime [18,20,24].

The stable mode locking of such an anomalously dispersive long fiber laser cavity is sharply contrary to several previous reports [37–39]. We thus numerically investigate the pulse evolution inside the cavity to determine the mechanism of the stable pulse generation, as summarized in Figs. 4(a)–4(d). In

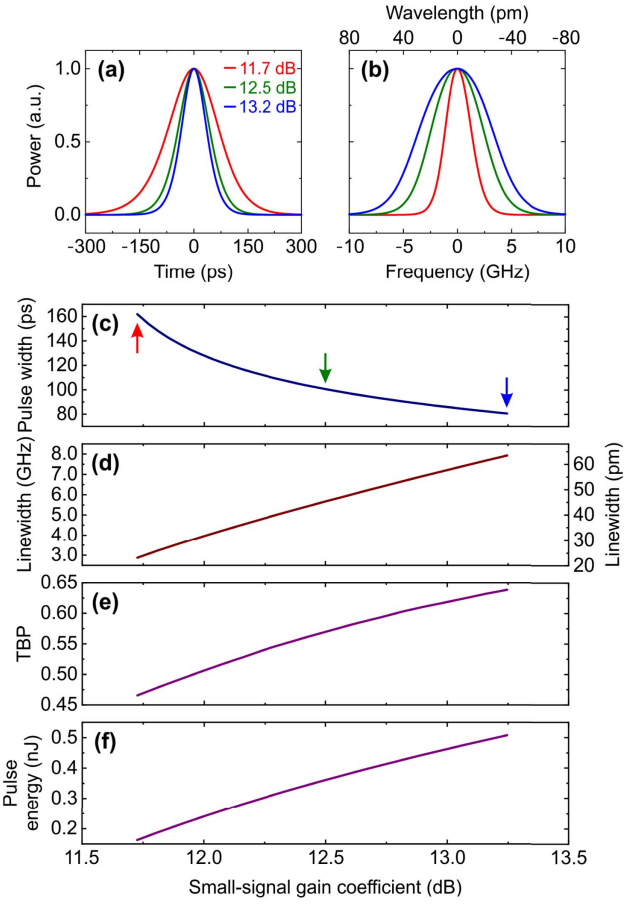

Fig. 3. Numerical modeling of mode-locked laser pulses. (a) Temporal pulse profiles and (b) pulse spectra at three different small-signal gain coefficients (11.7 dB for red, 12.5 dB for green, and 13.2 dB for blue); (c)–(f) calculated pulse parameters, (c) pulse width, (d) linewidth, (e) time–bandwidth product (TBP), and (f) pulse energy over a range of small-signal gain coefficient values. The three vertical arrows in (c) indicate the small-signal gain coefficients that correspond to the curves of respective colors in (a) and (b). The laser wavelength is fixed at 1550 nm for all calculations.

the temporal domain [Fig. 4(a)], the pulse width increases at the TBF, and this local pulse stretching is counterbalanced by the saturable absorption at the SESAM. It can be further seen that except at the TBF and the SESAM, the pulse width is nearly unchanged, the dispersion-induced pulse broadening being negligible, particularly at the long fiber delay line, due to the ultra-narrow linewidth of the laser pulses. As a result, the pulse width does not vary significantly during the cavity round trip, its relative change being less than 5% in our case for the entire working range of the small-signal gain coefficient. These results reveal that our MLFL is designed to operate in the dispersion-insensitive chirpless regime in which the spectral filtering at the TBF accompanies temporal pulse stretching rather than the conventional pulse-shortening action that is generally accompanied by much larger temporal breathing of pulses during the cavity round trip [40–42]. On the other hand, the linewidth [Fig. 4(b)] and the resulting TBP [Fig. 4(c)] increase monotonically as the pulse travels along the fiber delay line

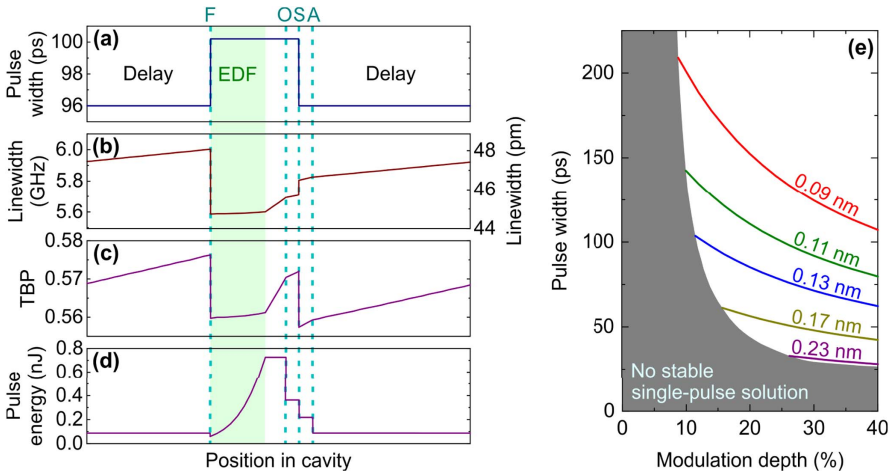

Fig. 4. Theoretical analysis of our ultra-narrow-linewidth dissipative soliton fiber laser. (a)–(d) Intracavity evolution of the pulse parameters: (a) pulse width, (b) linewidth, (c) time–bandwidth product (TBP), (d) pulse energy. F, bandpass filter; EDF, erbium-doped fiber; O, 50/50 output coupler; S, saturable absorber; A, attenuator. (e) Calculated pulse widths over a varying SESAM modulation depth for five different intracavity filter bandwidths (0.09, 0.11, 0.13, 0.17, and 0.23 nm). The gray region indicates where the stationary single-pulse solution does not exist. The small-signal gain coefficient is fixed at $g_0 = 12.5$ dB for all the calculations.

due to the SPM-induced frequency chirp. The linewidth also increases at the SESAM via the pulse-narrowing action and then decreases back at the TBF, which indicates that the SPM-induced spectral broadening at the fiber delay line and the pulse-shaping-induced spectral broadening at the SESAM are compensated by the spectral filtering at the TBF in the spectral domain. In addition, the pulse energy is maximized while the linewidth is nearly minimized immediately after the EDF, as shown in Figs. 4(b) and 4(d), and therefore it is reasonable to place a tapping coupler there to obtain the laser output. Furthermore, the placement order of the attenuator, fiber delay line, TBF, and EDF in Fig. 1 turns out to be very appropriate for the robust generation of the transform-limited single-soliton state against the SPM-induced pulse breakup. We note that direct experimental verification of the intracavity evolution of the pulse width is hindered because of the considerable uncertainty of several picoseconds in the pulse width measurement, as can be seen in Fig. 2(g), which is impacted significantly by the pulse timing jitter [43] that we will discuss in detail later.

In strong contrast to conventional soliton mode locking achieved via the balance between the nonlinearity and dispersion [40–42], our MLFL operates in the nearly dispersion-insensitive chirpless regime, where stable soliton formation relies on the subtle counterbalance among the actions of the TBF, SESAM, and in-fiber Kerr nonlinearity in both the temporal and spectral domains. We search for the criteria for the formation of such stable dissipative solitons in the long fiber laser cavity, in terms of the characteristics of the intracavity spectral filter and saturable absorber. Figure 4(e) displays the theoretically predicted pulse widths for a range of filter bandwidths and varying modulation depth of the saturable absorber. It is revealed that the filter bandwidth should be narrow enough to counteract the Kerr-induced SPM in the long fiber delay line. Our numerical calculation indicates that the filter bandwidth should be as narrow as ~0.24 nm (30 GHz) or less, which is even lower than those of typical commercially available dense-wavelength-division-multiplexing bandpass filters with a bandwidth of 0.4 nm (50 GHz) or 0.8 nm (100 GHz), to obtain a stable single-pulse state for an 80-m-long SMF delay line. In our experiments, we replace the intracavity TBF by another having a broader bandwidth of 0.4 nm, 0.8 nm, or higher, but we observe that the use of any alternative TBF does not yield stable mode locking. Furthermore, the modulation depth of a saturable absorber should be large enough to counterbalance the local pulse stretching at such a narrowband TBF. The use of a broader filter bandwidth yields a shorter pulse width, as shown in Fig. 4(e), which in turn requires a higher-modulation-depth saturable absorber for stable mode locking. Figure 4(e) suggests that a modulation depth of ~10% or higher is required in our case.

Next, we experimentally investigate the delay line dependence of the pulse parameters. In our experiments, the self-starting stable mode locking is readily achieved when the fiber delay line is sufficiently long (> ~ 40 m) to make the total cavity length greater than ~60 m (corresponding to a pulse repetition rate of 3.3 MHz). When the delay line length is less than ~40 m, self-starting mode locking does not occur, and instead we observe that the single-pulse state can be produced only by increasing the pump power to reach the multi-pulsing regime and then reducing it back to the single-pulse regime [26]. In this case, although a single-pulse solution exists, it is very difficult for the initial noisy background to progress directly into the single-pulse state due to the insufficient amount of nonlinear spectral broadening in the short delay line against the spectral filtering at the TBF. Thus, we need to increase the pump power to produce sufficient nonlinear spectral broadening, where the stable solution is a multi-pulse state rather than a single-pulse one, and then make use of the typical hysteresis behavior with respect to the direction of pump power scanning [26] to access a single-pulse state. As shown in Figs. 5(a)–5(d), the pump power threshold for the self-starting mode locking

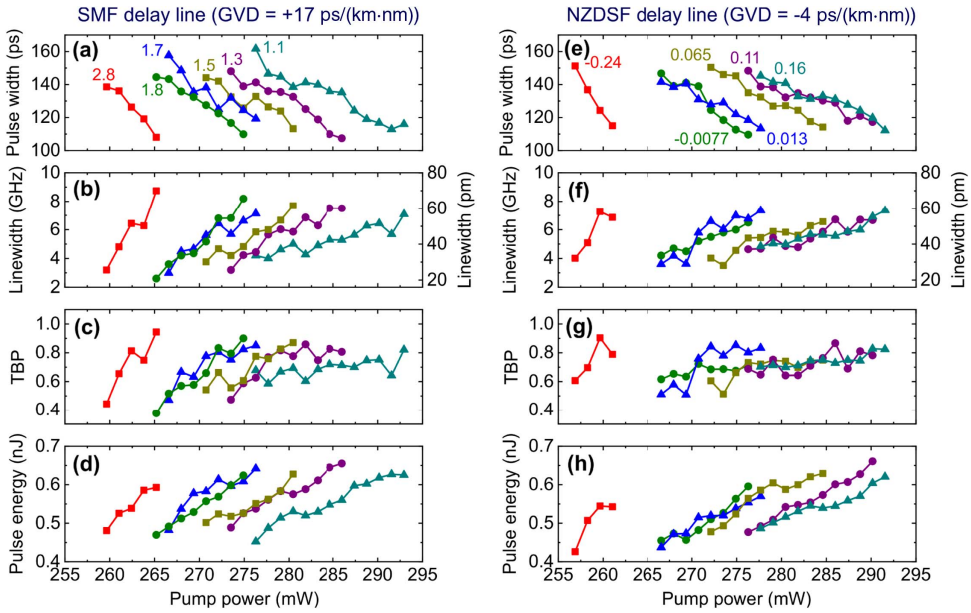

Fig. 5. Dependence of pulse parameters on the delay line length measured over a range of pump power values. (a)–(d) Measured pulse parameters, (a) pulse width, (b) linewidth, (c) time–bandwidth product (TBP), and (d) pulse energy for six different lengths of standard single-mode fiber (SMF) delay line (40, 50, 60, 70, 80, and 140 m), which yield net cavity dispersions of 1.1, 1.3, 1.5, 1.7, 1.8, and 2.8 ps/nm, respectively. (e)–(h) Measured pulse parameters, (e) pulse width, (f) linewidth, (g) TBP, and (h) pulse energy for six different lengths of non-zero dispersion-shifted fiber (NZDSF) delay line (40, 50, 60, 70, 80, and 140 m), which yield net cavity dispersions of 0.16, 0.11, 0.065, 0.013, −0.0079, and −0.24 ps/nm, respectively. The colored numbers in (a) and (e) indicate the net cavity dispersions in ps/nm. The laser wavelength is fixed at 1550 nm for all measurements.

increases with a shorter delay line because a higher pump power is required to create the amount of SPM-induced spectral broadening that is necessary to stabilize the pulsed state against the narrowband spectral filtering. Hence, a longer fiber cavity is beneficial for not only reduction of the pulse repetition rate but also stable self-starting mode locking when an ultra-narrowband filter is incorporated, which is in sharp contrast to conventional MLFLs, for which shorter cavity lengths are desirable for stable self-starting operation [44]. Moreover, as the delay line gets longer, the pulse parameters change more steeply with the pump power variation, because the amount of in-fiber SPM becomes more sensitive to the pump power. However, when the delay line is too long, the laser is more likely to enter the unstable multi-pulsing regime. We experimentally observe mode locking even at a repetition rate as low as ∼1.3 MHz (corresponding to a total cavity length of ∼160 m), which is particularly useful for nonlinear optics experiments that demand more intense pump pulses, although the operating pump power range becomes very narrow and the mode locking becomes somewhat unstable and easily broken by environmental perturbation.

The variation in delay line length also changes the cavity dispersion, and one may doubt whether the cavity dispersion change also has significant influence on the self-starting mode-locking operation and pulse properties. We thus check the cavity dispersion dependence of the pulse parameters. Here we replace the telecom SMF delay line with a non-zero dispersion-shifted fiber (NZDSF) with a normal dispersion of −4.0 ps/(km · nm) at a 1550 nm wavelength but a mode field diameter similar to that of SMF (10.4 μm for SMF and 9.1 μm for NZDSF) to maintain the amount of Kerr nonlinearity in the delay line. The net cavity dispersion can then be made weakly anomalous (far below +1 ps/nm) and even normal. We observe, however, that all the previously described experimental observations including the pulse parameters for each given pump power, the threshold pump powers and required delay line lengths for self-starting operation, and the multi-pulsing behaviors beyond the single-pulse regime are almost the same as in the case where an SMF delay line is used, as shown in Figs. 5(e)–5(h). These experimental results indicate that the formation of dissipative solitons in our case is indeed nearly insensitive to both the magnitude and sign of the cavity dispersion. The small difference in pulse parameters between the two types of delay line is attributed to the fact that they have slightly different Kerr nonlinearities arising from the different mode field diameters, and there exists a splice loss of ∼0.2 dB for each SMF–NZDSF interface that might have an effect on the laser pulses.

Finally, we examine the laser wavelength tunability by adjusting the center wavelength of the intracavity TBF. As shown in Figs. 6(a)–6(e), the laser wavelength can be tuned over a wide range of 34.3 nm (1529.3–1563.6 nm) that covers almost the entire telecom C-band, stable mode locking being maintained without pulse breakup, while the pulse parameters vary gradually with the wavelength tuning mainly due to the spectral dependence of the EDF gain and SESAM absorption. The demonstrated wavelength tuning range is much broader than in the relevant previous works at the telecom band [27–29]. Such a markedly wide pulse-breakup-free wavelength tunability is also achieved for the case of NZDSF delay line, which

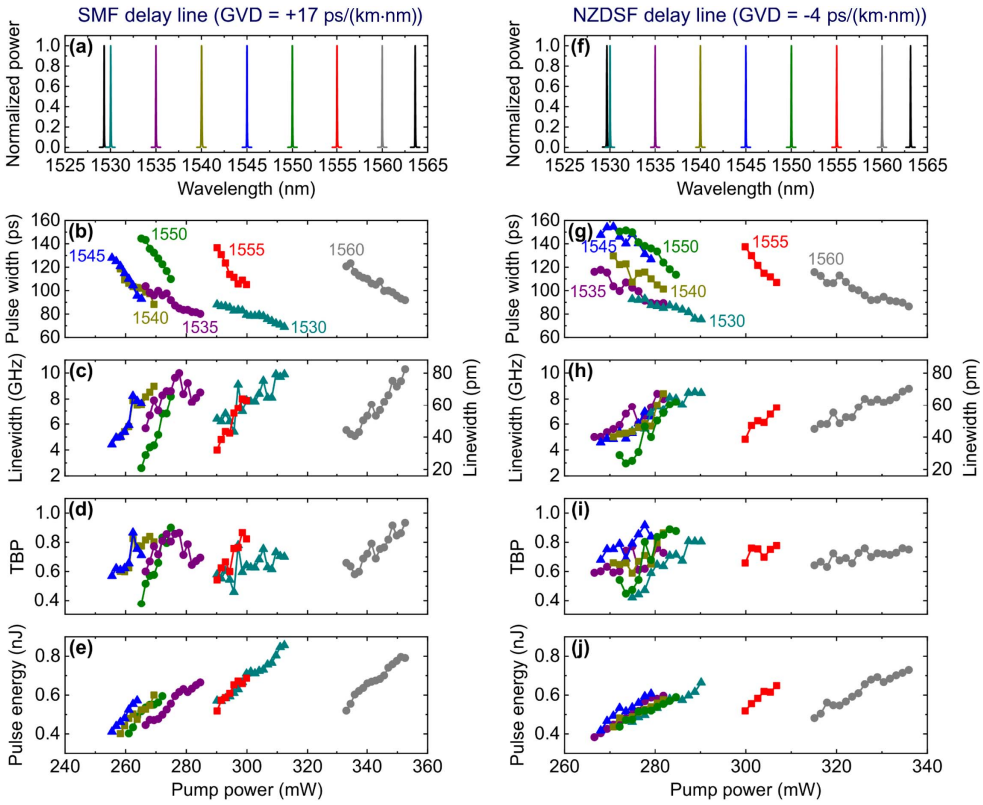

Fig. 6. Characteristics of laser wavelength tuning. (a) Normalized optical output spectra of the laser with an 80-m-long single-mode fiber (SMF) delay line obtained by a grating-based optical spectrum analyzer (OSA). The laser wavelength can be tuned without pulse breakup over a 34.3 nm range (1529.3–1563.6 nm) by changing the center wavelength of the intracavity tunable bandpass filter and the pump power. (b)–(e) Pump power dependence of pulse parameters, (b) pulse width, (c) linewidth, (d) time–bandwidth product (TBP), and (e) pulse energy measured at six different laser wavelengths. (f) Normalized optical output spectra of the laser with an 80-m-long non-zero dispersion-shifted fiber (NZDSF) delay line obtained by a grating-based OSA. The laser wavelength can be tuned without pulse breakup over a 33.4 nm range (1529.7–1563.1 nm). (g)–(j) Pump power dependence of pulse parameters, (g) pulse width, (h) linewidth, (i) TBP, and (j) pulse energy measured at six different laser wavelengths. The colored numbers in (b) and (g) indicate the laser wavelengths in nm, which correspond to the colors of the laser spectra in (a) and (e), respectively. The laser spectra in black in (a) and (f) are obtained close to the lower and upper bounds of the wavelength tuning range.

exhibits a similar tuning range of 33.4 nm (1529.7–1563.1 nm), as shown in Figs. 6(f)–6(j), further verifying the dispersion insensitiveness of dissipative soliton formation. The pulse width becomes smaller as the laser wavelength is tuned shorter (i.e., approaching 1530 nm), which can be understood from the fact that the EDF gain increases at shorter wavelengths, and the SPM-induced spectral broadening and the resulting pulse width shortening at the TBF are enhanced. The laser needs to be pumped harder to self-start at longer laser wavelengths (i.e., toward 1560 nm), which is mainly because both the non-saturable absorption and modulation depth of the SESAM diminish at longer wavelengths beyond ~1560 nm, which weakens the pulse shaping function at the SESAM.

While all the experimentally observed dependences of pulse characteristics on the laser cavity parameters agree well with the results from numerical analysis, there are some small discrepancies between them. In particular, while the numerical modeling predicts that the pulse width can decrease to 80 ps as the pump power rises within the experimentally available range, in actual experiments the pulse width does not reduce below ~100 ps. This is because the laser enters the multi-pulse regime or becomes unstable as the pump power is increased above a certain level (typically ~300 mW in our case) [26], which is attributed to the fact that the gain–loss balance that yields stable single-soliton operation is broken in the high-gain regime due to the strong nonlinear phase modulation in the fiber [32,33] and inverse saturable absorption at the SESAM [45].

It is worthwhile to add a further remark on the timing jitter that can contribute significantly to the uncertainty in the pulse width measurement [Fig. 2(g)]. It is known that in mode-locked lasers, the quantum noise introduced by gains and losses affects the pulse timing. In particular, when a single pulse circulates in the laser cavity, as in our case, the timing jitter produced by the fundamental quantum noise is proportional to the square of the pulse width, although it is also inversely proportional to the cavity round-trip time [43], which is beneficial in our long-length cavity. We measure the timing jitter power spectrum, as shown in Fig. 7(a), based on the electro-optic phase detection method [46] that incorporates a Sagnac loop fiber interferometer [47] and a stable microwave source. The microwave is phase locked to the laser pulse train by using a 15-kHz-bandwidth phase-locked loop. The timing jitter power

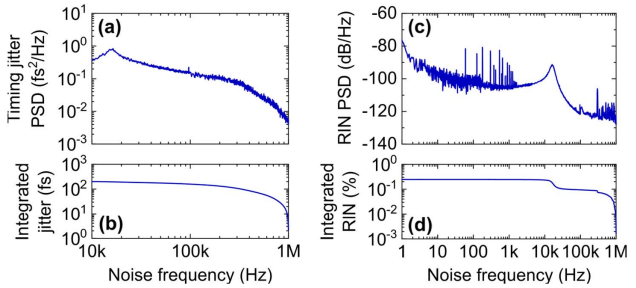

Fig. 7. Characteristics of the laser noise. (a) Timing jitter power spectrum, (b) integrated timing jitter, (c) relative intensity noise (RIN) power spectrum, (d) integrated RIN. In all measurements, we fix the pump power as 265.2 mW, the single-mode fiber delay line length as 80 m, and the laser wavelength as 1550 nm. PSD, power spectral density.

spectrum is then integrated over a frequency range of 15 kHz to 1 MHz to yield a root-mean-square (RMS) timing jitter of 196 fs [Fig. 7(b)]. We also measure the fluctuation of the pulse repetition rate without the phase locking to the microwave by using a radio frequency counter with a 1 s gate time, which corresponds to the absolute timing jitter. The uncertainty of the repetition rate is measured as ~6 Hz, which corresponds to an absolute timing jitter of ~1.5 ps. These results indicate that the absolute timing jitter is produced primarily by the low-frequency environmental perturbations on the laser system rather than the quantum noise. Such environmental perturbations can directly give rise to the fluctuation in the laser pulse envelope (i.e., pulse width) as well, which further increases the uncertainty in the pulse width measurement. Future research would be necessary to suppress the timing jitter via additional active pulse stabilization [48] for the experimental verification of the intracavity pulse evolution [Fig. 4(a)], as well as for applications to optical precision metrology.

We also measure the relative intensity noise (RIN) of the laser output using a 1-MHz-bandwidth photodetector [48], as shown in the RIN power spectrum of Fig. 7(c). The pronounced peak around 15 kHz is attributed to the laser relaxation oscillation, which normally appears in SESAM-based MLFLs. The RIN power spectrum is integrated over a frequency range of 1 Hz to 1 MHz to yield an RMS RIN of 0.25% [Fig. 7(d)]. We emphasize that the measured noise level indicates the sufficiently high stability and practicability of our laser system, even though it is operated at relatively high pump powers and low repetition rates (i.e., long fiber cavity lengths) and possesses intrinsic mechanical instability at the SESAM–fiber interface.

Finally, while we use a SESAM with a fixed modulation depth value, further experimental investigation of the influence of modulation depth might be valuable for validation of our theoretical prediction in Fig. 4(e). While we show experimentally that nonlinear-polarization-rotation-based passive mode locking of a long fiber laser cavity cannot be achieved in our case even with the use of a 0.11-nm-bandwidth TBF, as well as with a higher-bandwidth one, this observation can hardly be regarded as firm evidence that validates Fig. 4(e), particularly at low modulation depths. Such an experimental study could be carried out by exploiting a saturable absorber with an adjustable modulation depth, such as an electrically tunable graphene saturable absorber [49].

3. CONCLUSION

In conclusion, widely tunable ultra-narrow-linewidth nearly transform-limited dissipative solitons can be generated with low repetition rates at the telecom band from a suitably designed long-cavity MLFL. Careful selection and combination of an intracavity spectral filter, a saturable absorber, and a fiber delay line critically allow us to access a nearly dispersion-insensitive chirpless dissipative soliton mode-locking regime, where self-starting stable single-soliton generation can be achieved even from a highly anomalously dispersive long fiber laser cavity (>100 m) over a notably wide tuning range of laser wavelengths (1529.7–1563.1 nm) covering almost the entire telecom C-band. Our experimental demonstration and rigorous numerical modeling reveal that the subtle counterbalancing of a significantly narrow filter bandwidth, a sufficiently deep saturable absorption, and an appropriately strong Kerr nonlinearity accumulated in the long fiber cavity, in both the temporal and spectral domains, is the crucial mechanism in achieving this dissipative soliton generation without requiring cavity dispersion management. The unique combination of highly attractive pulse properties including the widely tunable laser wavelength (>34 nm), ultra-narrow linewidth on the order of gigahertz, variable pulse width around ~100 ps, and low repetition rate at a few megahertz cannot be efficiently attained by either conventional ultrafast mode-locked soliton fiber lasers or electro-optically intensity-modulated laser light, and thus our work may open up exciting new applications. For instance, a master oscillator power amplifier system that employs our pulsed laser as an oscillator might find immediate application as an idealized pump source for highly efficient nonlinear frequency conversion and nonclassical light generation in the long-length microphotonic/nanophotonic waveguide systems that have been rapidly attracting attention [8–17]. Compared to the case of typical nonlinear optical crystals, observation of high-efficiency nonlinear optical phenomena in microphotonic/nanophotonic long waveguide systems requires a pulsed pump source with a narrower linewidth and a longer temporal duration to fully exploit the considerable interaction lengths. We emphasize that our laser system can function as an idealized pump source for a tightly light-confining nanophotonic waveguide system whose length is on the order of 10 mm or larger [50,51], and which possesses a narrow phase-matching bandwidth (up to 100 pm) and a large group-velocity mismatch (up to 10 ps/mm). Furthermore, the low repetition rate is more favorable for efficient amplification of pulse energies, which is also highly desired for high-quality nonlinear imaging and spectroscopy [20]. Our study on the control of the properties of dissipative solitons might also offer new possibilities for engineering complex pulse-to-pulse interactions in dissipative multi-soliton systems [52–54].

Funding. National Research Foundation of Korea (NRF-2019R1A2C2088839, NRF-2019R1H1A2079908).

Acknowledgment. We thank J. Kim for his generous permission giving us access to the experimental apparatus for the measurement of the timing jitter and relative intensity noise in his laboratory.

Disclosures. The authors declare no conflicts of interest.

REFERENCES

1. W. Fu, L. G. Wright, P. Sidorenko, S. Backus, and F. W. Wise, "Several new directions for ultrafast fiber lasers," Opt. Express **26**, 9432–9463 (2018).
2. S. T. Le, V. Aref, and H. Buelow, "Nonlinear signal multiplexing for communication beyond the Kerr nonlinearity limit," Nat. Photonics **11**, 570–576 (2017).
3. J. M. Lukens and P. Lougovski, "Frequency-encoded photonic qubits for scalable quantum information processing," Optica **4**, 8–16 (2017).
4. C. Reimer, M. Kues, P. Roztocki, B. Wetzel, F. Grazioso, B. E. Little, S. T. Chu, T. Johnston, Y. Bromberg, L. Caspani, D. J. Moss, and R. Morandotti, "Generation of multiphoton entangled quantum states by means of integrated frequency combs," Science **351**, 1176–1180 (2016).
5. C. Xu and F. W. Wise, "Recent advances in fiber lasers for nonlinear microscopy," Nat. Photonics **7**, 875–882 (2013).
6. D. D. Hickstein, D. R. Carlson, H. Mundoor, J. B. Khurgin, K. Srinivasan, D. Westly, A. Kowligy, I. I. Smalyukh, S. A. Diddams, and S. B. Papp, "Self-organized nonlinear gratings for ultrafast nanophotonics," Nat. Photonics **13**, 494–499 (2019).
7. G. Wrigge, I. Gerhardt, J. Hwang, G. Zumofen, and V. Sandoghdar, "Efficient coupling of photons to a single molecule and the observation of its resonance fluorescence," Nat. Phys. **4**, 60–66 (2008).
8. J. Yuan, X. Sang, Q. Wu, G. Zhou, F. Li, X. Zhou, C. Yu, K. Wang, B. Yan, Y. Han, H. Y. Tam, and P. K. A. Wai, "Enhanced intermodal four-wave mixing for visible and near-infrared wavelength generation in a photonic crystal fiber," Opt. Lett. **40**, 1338–1341 (2015).
9. M. I. M. A. Khudus, T. Lee, F. De Lucia, C. Corbari, P. Sazio, P. Horak, and G. Brambilla, "All-fiber fourth and fifth harmonic generation from a single source," Opt. Express **24**, 21777–21793 (2016).
10. Y. Wang, T. Lee, F. De Lucia, M. I. M. A. Khudus, P. J. A. Sazio, M. Beresna, and G. Brambilla, "All-fiber sixth harmonic generation of deep UV," Opt. Lett. **42**, 4671–4674 (2017).
11. X. Guo, C.-L. Zou, and H. X. Tang, "Second-harmonic generation in aluminum nitride microrings with 2500%/W conversion efficiency," Optica **3**, 1126–1131 (2016).
12. S. Signorini, M. Mancinelli, M. Borghi, M. Bernard, M. Ghulinyan, G. Pucker, and L. Pavesi, "Intermodal four-wave mixing in silicon waveguides," Photon. Res. **6**, 805–814 (2018).
13. J. B. Surya, X. Guo, C.-L. Zou, and H. X. Tang, "Efficient third-harmonic generation in composite aluminum nitride/silicon nitride microrings," Optica **5**, 103–108 (2018).
14. M. Corona, K. Garay-Palmett, and A. B. U'Ren, "Experimental proposal for the generation of entangled photon triplets by third-order spontaneous parametric downconversion in optical fibers," Opt. Lett. **36**, 190–192 (2011).
15. A. Dot, A. Borne, B. Boulanger, K. Bencheikh, and J. A. Levenson, "Quantum theory analysis of triple photons generated by a $\chi^{(3)}$ process," Phys. Rev. A **85**, 023809 (2012).
16. S. Afshar, V, M. A. Lohe, T. Lee, T. M. Monro, and N. G. R. Broderick, "Efficient third and one-third harmonic generation in nonlinear waveguides," Opt. Lett. **38**, 329–331 (2013).
17. J. W. Silverstone, D. Bonneau, J. L. O'Brien, and M. G. Thompson, "Silicon quantum photonics," IEEE J. Sel. Top. Quantum Electron. **22**, 390–402 (2016).
18. M. Baumgartl, J. Abreu-Afonso, A. Dìez, M. Rothhardt, J. Limpert, and A. Tünnermann, "Environmentally stable picosecond Yb fiber laser with low repetition rate," Appl. Phys. B **111**, 39–43 (2013).
19. A. Agnesi, L. Carrá, F. Pirzio, R. Piccoli, and G. Reali, "Low repetition rate, hybrid fiber/solid-state, 1064 nm picosecond master oscillator power amplifier laser system," J. Opt. Soc. Am. B **30**, 2960–2965 (2013).
20. M. Baumgartl, T. Gottschall, J. Abreu-Afonso, A. Díez, T. Meyer, B. Dietzek, M. Rothhardt, J. Popp, J. Limpert, and A. Tünnermann, "Alignment-free, all-spliced fiber laser source for CARS microscopy based on four-wave-mixing," Opt. Express **20**, 21010–21018 (2012).
21. A. Agnesi, L. Carrà, C. Di Marco, R. Piccoli, and G. Reali, "Fourier-limited 19-ps Yb-fiber seeder stabilized by spectral filtering and tunable between 1015 and 1085 nm," IEEE Photon. Technol. Lett. **24**, 927–929 (2012).
22. J. Liu, J. Xu, and P. Wang, "High repetition-rate narrow bandwidth SESAM mode-locked Yb-doped fiber lasers," IEEE Photon. Technol. Lett. **24**, 539–541 (2012).
23. Y. Wang, B.-L. Lu, X. Y. Qi, L. Hou, J. Kang, K.-X. Huang, X.-Q. Feng, D.-L. Zhang, H.-W. Chen, and J.-T. Bai, "Environmentally stable pulse energy-tunable picosecond fiber laser," IEEE Photon. Technol. Lett. **29**, 150–153 (2017).
24. Q. Lu, J. Ma, D. Duan, X. Lin, and Q. Mao, "Reducing the pulse repetition rate of picosecond dissipative soliton passively mode-locked fiber laser," Opt. Express **27**, 2809–2816 (2019).
25. C. M. Harvey, F. Yu, J. C. Knight, W. J. Wadsworth, and P. J. Almeida, "Reduced repetition rate Yb^{3+} mode-locked picosecond fiber laser with hollow core fiber," IEEE Photon. Technol. Lett. **28**, 669–672 (2016).
26. S. Boivinet, J.-B. Lecourt, Y. Hernandez, A. A. Fotiadi, M. Wuilpart, and P. Mégret, "All-fiber 1-μm PM mode-lock laser delivering picosecond pulses at sub-MHz repetition rate," IEEE Photon. Technol. Lett. **26**, 2256–2259 (2014).
27. I. A. Litago, D. Leandro, M. Á. Quintela, R. A. Pérez-Herrera, M. López-Amo, and J. M. López-Higuera, "Tunable SESAM-based mode-locked soliton fiber laser in linear cavity by axial-strain applied to an FBG," J. Lightwave Technol. **35**, 5003–5009 (2017).
28. T. Wang, Z. Yan, C. Mou, Z. Liu, Y. Liu, K. Zhou, and L. Zhang, "Narrow bandwidth passively mode locked picosecond erbium doped fiber laser using a 45° tilted fiber grating device," Opt. Express **25**, 16708–16714 (2017).
29. M. Kues, C. Reimer, B. Wetzel, P. Roztocki, B. E. Little, S. T. Chu, T. Hansson, E. A. Viktorov, D. J. Moss, and R. Morandotti, "Passively mode-locked laser with an ultra-narrow spectral width," Nat. Photonics **11**, 159–162 (2017).
30. P. Grelu and N. Akhmediev, "Dissipative solitons for mode-locked laser," Nat. Photonics **6**, 84–92 (2012).
31. J. Lægsgaard, "Control of fibre laser mode-locking by narrow-band Bragg gratings," J. Phys. B **41**, 095401 (2008).
32. X. Zhang, F. Li, K. Nakkeeran, J. Yuan, Z. Kang, J. N. Kutz, and P. K. A. Wai, "Impact of spectral filtering on multipulsing instability in mode-locked fiber lasers," IEEE J. Sel. Top. Quantum Electron. **24**, 1101309 (2018).
33. M. Alsaleh, T. Uthayakumar, E. T. Felenou, P. T. Dinda, P. Grelu, and K. Porsezian, "Pulse breaking through spectral filtering in dispersion-managed fiber lasers," J. Opt. Soc. Am. B **35**, 276–283 (2018).
34. M. S. Kang, N. Y. Joly, and P. St. J. Russell, "Passive mode-locking of fiber ring laser at the 337th harmonic using gigahertz acoustic core resonances," Opt. Lett. **38**, 561–563 (2013).
35. H. A. Haus, "Mode-locking of lasers," IEEE J. Sel. Top. Quantum Electron. **6**, 1173–1185 (2000).
36. G. Agrawal, *Nonlinear Fiber Optics*, 5th ed. (Academic, 2013).
37. X. Li, X. Kiu, X. Hu, L. Wang, H. Lu, Y. Wang, and W. Zhao, "Long-cavity passively mode-locked fiber ring laser with high-energy rectangular-shape pulses in anomalous dispersion regime," Opt. Lett. **35**, 3249–3251 (2010).
38. X. Zhang, C. Gu, G. Chen, B. Sun, L. Xu, A. Wang, and H. Ming, "Square-wave pulse with ultra-wide tuning range in a passively mode-locked fiber laser," Opt. Lett. **37**, 1334–1336 (2012).
39. L. A. Rodrigues-Morales, I. Armas-Rivera, B. Ibarra-Escamilla, O. Pottiez, H. Santiago-Hernandez, M. Durán-Sánchez, M. V. Andrés, and E. A. Kuzin, "Long cavity ring fiber mode-locked laser with decreased net value of nonlinear polarization rotation," Opt. Express **27**, 14030–14040 (2019).
40. A. Chong, J. Buckley, W. Renninger, and F. Wise, "All-normal-dispersion femtosecond fiber laser," Opt. Express **14**, 10095–10100 (2006).
41. A. Chong, W. H. Renninger, and F. W. Wise, "Properties of normal-dispersion femtosecond fiber lasers," J. Opt. Soc. Am. B **25**, 140–148 (2008).

42. W. H. Renninger, A. Chong, and F. W. Wise, "Dissipative solitons in normal-dispersion fiber lasers," Phys. Rev. A **77**, 023814 (2008).
43. R. Paschotta, "Timing jitter and phase noise of mode-locked fiber lasers," Opt. Express **18**, 5041–5054 (2010).
44. F. Krausz, T. Brabec, and C. Spielmann, "Self-starting passive mode locking," Opt. Lett. **16**, 235–237 (1991).
45. R. Grange, M. Haiml, R. Paschotta, G. J. Spühler, L. Krainer, M. Golling, O. Ostinelli, and U. Keller, "New regime of inverse saturable absorption for self-stabilizing passively mode-locked lasers," Appl. Phys. B **80**, 151–158 (2005).
46. M. Endo, T. D. Shoji, and T. R. Schibli, "High-sensitivity optical to microwave comparison with dual-output Mach-Zehnder modulators," Sci. Rep. **8**, 4388 (2018).
47. K. Jung and J. Kim, "Sub-femtosecond synchronization of microwave oscillators with mode-locked Er-fiber lasers," Opt. Lett. **37**, 2958–2960 (2012).
48. J. Kim and Y. Song, "Ultralow-noise mode-locked fiber lasers and frequency combs: principles, status, and applications," Adv. Opt. Photon. **8**, 465–540 (2016).
49. E. J. Lee, S. Y. Choi, H. Jeong, N. H. Park, W. Yim, M. H. Kim, J.-K. Park, S. Son, S. Bae, S. J. Kim, K. Lee, Y. H. Ahn, K. J. Ahn, B. H. Hong, J.-Y. Park, F. Rotermund, and D.-I. Yeom, "Active control of all-fibre graphene devices with electrical gating," Nat. Commun. **6**, 6851 (2015).
50. V. Grubsky and A. Savchenko, "Glass micro-fibers for efficient third harmonic generation," Opt. Express **13**, 6798–6806 (2005).
51. J. Lægsgaard, "Theory of surface second-harmonic generation in silica nanowires," J. Opt. Soc. Am. B **27**, 1317–1324 (2010).
52. R. Weill, A. Bekker, V. Smulakovsky, B. Fischer, and O. Gat, "Noise-mediated Casimir-like pulse interaction mechanism in lasers," Optica **3**, 189–192 (2016).
53. K. Sulimany, O. Lib, G. Masri, A. Klein, M. Fridman, P. Grelu, O. Gat, and H. Steinberg, "Bidirectional soliton rain dynamics induced by Casimir-like interactions in a graphene mode-locked fiber laser," Phys. Rev. Lett. **121**, 133902 (2018).
54. K. S. Lee, C. K. Ha, K. J. Moon, D. S. Han, and M. S. Kang, "Tailoring of multi-pulse dynamics in mode-locked laser via optoacoustic manipulation of quasi-continuous-wave background," Commun. Phys. **2**, 141 (2019).